

Correlative angstrom-scale microscopy and spectroscopy of graphite–water interfaces

Lalith Krishna Samanth Bonagiri^{1,2†}, Diana M. Arvelo^{3†}, Fujia Zhao^{1,4†}, Jaehyeon Kim^{1,4}, Qian Ai^{1,4}, Shan Zhou^{1,4}, Kaustubh S. Panse^{1,4}, Ricardo Garcia^{3*}, and Yingjie Zhang^{1,4,5*}

1. Materials Research Laboratory, University of Illinois, Urbana, IL 61801, USA
2. Department of Mechanical Science and Engineering, University of Illinois, Urbana, IL 61801, USA
3. Instituto de Ciencia de Materiales de Madrid, CSIC, Madrid 28049, Spain
4. Department of Materials Science and Engineering, University of Illinois, Urbana, IL 61801, USA
5. Beckman Institute for Advanced Science and Technology, University of Illinois, Urbana, IL 61801, USA

†These authors contributed equally

*Correspondence to: yjz@illinois.edu (Y.Z.) and r.garcia@csic.es (R.G.)

Abstract: Water at solid surfaces is key for many processes ranging from biological signal transduction to membrane separation and renewable energy conversion. However, under realistic conditions, which often include environmental and surface charge variations, the interfacial water structure remains elusive. Here we overcome this limit by combining three-dimensional atomic force microscopy and interface-sensitive Raman spectroscopy to characterize the graphite–water interfacial structure in situ. Through correlative analysis of the spatial liquid density maps and vibrational peaks within ~ 2 nm of the graphite surface, we find the existence of two interfacial configurations at open circuit potential, a transient state where pristine water exhibits strong hydrogen bond (HB) breaking effects, and a steady state with hydrocarbons dominating the interface and weak HB breaking in the surrounding water. At sufficiently negative potentials, both states transition into a stable structure featuring pristine water with a broader distribution of HB configurations. Our three-state model resolves many long-standing controversies on interfacial water structure.

Water is essential in biology and in technology. Many water-mediated processes depend critically on the structure of solid–water interfaces, such as the electrode–water interface in electrochemical systems, membrane–water interface of biological cells, and the semiconductor–water interface in biosensing and photocatalysis^{1–4}. Bulk water has a well-known configuration in the form of a dynamic HB network⁵. In contrast, the structure of water near a solid surface (interfacial water) has been a subject of intense debates and controversies. Even the description of ideal interfaces, such as pure water next to a crystalline solid surface, is a challenge for state-of-the-art atomistic simulations^{1,3}. In real life, various salt and organic species, either intentionally added or adventitious, inevitably exist in water. If the concentration of these impurities is low, the bulk water structure is expected to remain unaffected⁵. However, at the interfacial region (within ~ 2 nm from a solid surface), even trace amounts of salt or organic species from the bulk may adsorb or accumulate to a high concentration^{1,6–8}. As a result, the solid–water interfacial structure is influenced by several factors including the steric hard wall effect, hydrophobicity, electric field,

and surface adhesion. The large variety of possible molecular species and interactions make the solid–water interface inherently complex.

In the past three decades, many techniques have been developed or implemented to characterize the interfacial water structure^{6,9–22}. These methods can be broadly classified into three categories: interface-sensitive spectroscopies (e.g., sum frequency generation, X-ray absorption, and surface-enhanced Raman)^{17–19,23,24}, scattering methods (using X-ray or neutron)^{20–22}, and real-space imaging by three-dimensional atomic force microscopy (3D-AFM)^{6,9–16}. The results have been interpreted via two distinct models. One assumes that pristine water molecules occupy the interface, as supported by a lack of non-water peaks in spectroscopies or a ~ 3 Å liquid layer spacing in 3D-AFM or X-ray/neutron scattering (intermolecular distance of bulk water is ~ 3 Å)^{9,11,13,15,19,20}. The other model hypothesizes that adventitious airborne or liquid-borne species (likely hydrocarbons) dominate the 1–2 nm interfacial region. This “non-pristine” model is based on the observation of hydrocarbon-related vibrational peaks in spectroscopies, a 4–5 Å interlayer distance identified by 3D-AFM, or a significant reduction of water density at the interface measured by X-ray or neutron reflectivity^{6,21,25–27}. These discrepancies cannot be attributed to differences in the solid structure, as they occur for many commonly used substrates including Au, graphite, graphene, and self-assembled monolayers (Supplementary Tables 1–4).

In the presence of surface charges or an electric field, the response of interfacial water structure is also highly controversial, with existing reports claiming markedly different degrees of HB reconfiguration or change in the interlayer spacing^{12,16–19,28} (Supplementary Tables 1–4).

The above controversies in interfacial water structure may stem from several factors. One possibility is the variation in sample conditions across different labs, influenced by differences in water purity, preparation methods, and/or ambient condition. Another factor is the limited amount and type of information that can be extracted from each individual characterization method; these limits make it difficult to accurately determine interfacial structures using any single technique.

To resolve the discrepancies of solid–water interfaces, we combined the atomic-resolution imaging method 3D-AFM (Fig. 1a,b) with shell-isolated nanoparticle-enhanced Raman spectroscopy (SHINERS)^{16,19,29} (Fig. 1c,d). Among the existing methods to study solid–water interfaces, 3D-AFM and SHINERS are both uniquely sensitive to the same 1–2 nm thick interfacial liquid region above flat substrates^{19,30–32}. The capability of SHINERS to detect graphite–water interfaces is further verified by the observation of graphite G band and the strong potential-dependence of the overall signal, as shown later in this article. Therefore, the combination of these two methods enables a direct and reliable integration of the complementary spatial density profiles (from 3D-AFM) and chemical bonding configurations (from SHINERS), thus providing comprehensive information on the interfacial liquid structure.

Among the existing interfacial systems, carbon–water interfaces are crucial for a wide range of applications, including energy storage, electrocatalysis, biosensing, water desalination, and more^{33–36}. Here we use highly oriented pyrolytic graphite (HOPG) as the model carbon electrode system, which has a flat, homogeneous basal plane surface enabling a reliable comparison of imaging and spectroscopy data. Additionally, the simple mechanical exfoliation method for surface preparation ensures reproducible measurements in different labs. The experiments were

carried out independently over a four-year period under different environmental conditions in two locations, Madrid (Spain) and Urbana (IL, USA). A combination of 16 separate sets of 3D-AFM and 4 sets of SHINERS measurements are reported here; each measurement lasted for 1–2 days, during which the potential-dependence and time evolution of interfacial liquids were thoroughly examined across multiple sample spots. A comprehensive analysis of all the data together reveals three types of interfacial configurations: a transient pristine water state with strong HB breaking near open circuit potential (OCP) (State 1), a stable hydrocarbon-dominated structure with weak HB breaking of water near OCP (State 2), and a stable pristine water state with a broad distribution of HB configurations at sufficiently negative potentials (State 3). These states transition between each other due to either time evolution or potential modulation.

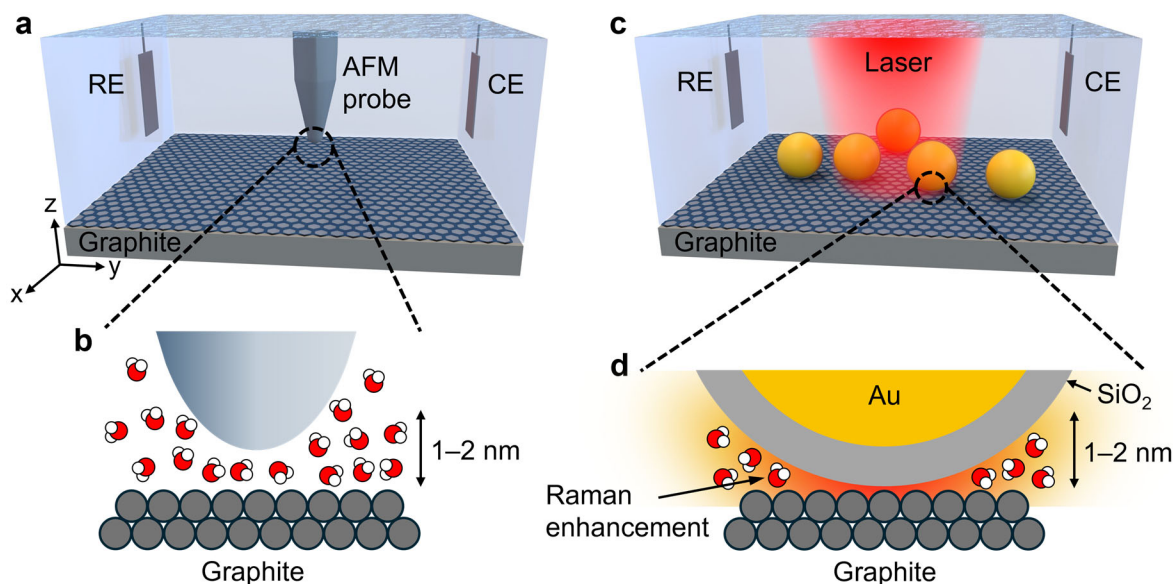


Fig. 1 | Schematic of the measurement setups. **a**, Illustration of a 3D-AFM probe operating inside an electrochemical cell with a graphite working electrode. RE: reference electrode; CE: counter electrode. **b**, Enlarged view of the graphite–water interface, where the AFM probe captures the interfacial water density distribution via force mapping. **c**, Diagram of the SHINERS setup using a similar electrochemical cell. Au/SiO₂ core/shell nanoparticles are dispersed on the graphite electrode surface. A laser source is used to induce Raman scattering. **d**, Expanded view of the interfacial region, where Raman signal of the water molecules within 1–2 nm from the graphite surface is enhanced.

Interfacial configurations at OCP

In this work, OCP values for all the liquid electrolytes were similar, and determined to be 0.17 ± 0.15 V vs Ag/AgCl. For both 3D-AFM and SHINERS, results measured within the range of 0–0.4 V vs Ag/AgCl did not show observable differences. Therefore, potentials within 0–0.4 V vs Ag/AgCl are all regarded as OCP.

3D-AFM was performed at OCP on freshly cleaved HOPG immersed in pure water. We imaged a volume of at least $5 \text{ nm} \times 5 \text{ nm} \times 1.5 \text{ nm}$ along x, y (in-plane), and z (out-of-plane) directions at each location, to ensure statistical significance. x–z maps of pure water at HOPG surface reveals

multiple discrete layers, where the interlayer spacing evolved from the initial value of ~ 3 Å to 4–5 Å within about one hour (Fig. 2a,b and Supplementary Fig. 1a–c). These results are consistent with previous reports^{6,25,37}. As explained before, ~ 3 Å corresponds to pristine hydration layers, while 4–5 Å is likely due to the accumulation of adventitious species whose exact nature remains unknown to date^{6,25,37}. The average force vs z curves extracted from the x – z maps (Fig. 2a), shown in Fig. 2b, top panel, confirmed the same layered structures with damped oscillations as typical for interfacial liquids³⁰. Most of the force curves obtained in this work exhibited at least two peaks under all sample and probe conditions. Whenever more than two peaks were identified, the upper layers showed similar interlayer distances as the 1st to 2nd layer (Supplementary Fig. 2). Therefore, the 1st–2nd layer distance (d_{12}) is a reliable experimental descriptor of the observed interfacial liquid density profile. This distance will be used for statistically significant analysis throughout this work.

For the rest of the article, although full 3D imaging was performed for each AFM result, we only show the individual and average force curves in the figures to avoid redundancy and highlight the evolution of d_{12} .

3D-AFM of electrolyte solutions, including K_2SO_4 in water (0.01–0.2 M) and KCl in water (0.1 M), revealed similar layered interfacial liquid structures with nearly the same time evolution of d_{12} (Fig. 2b and Supplementary Fig. 1). These results underline the reproducibility of the observed interfacial structural evolution. Furthermore, the findings are largely independent of the salt species and concentration. We thus rule out the possibility that changes in interlayer spacing are induced by interfacial ion aggregation. This interpretation is consistent with prior reports that showed the salt-independence of hydration layer spacings in dilute solutions (<1 M)^{9,11,30,38,39}. Note that the distance between the first peak and the substrate exhibits large variations among most of the results, which have been previously observed in aqueous solutions^{10,14,40} and attributed to the fluctuations in the hydration condition of the end of the AFM probe, rather than the intrinsic liquid structure⁴¹. d_{12} , on the other hand, is highly reproducible and independent of the AFM probe, as reported before^{6,25,30,40} and evident in the significant amounts of data shown in this work (Supplementary Figs. 1–12 and Tables 5 and 6).

We further interrogated the chemical composition of the HOPG–water interface using SHINERS. As shown in Fig. 1c,d, the substrate for SHINERS consists of Au/SiO₂ core/shell nanoparticles deposited on HOPG (Supplementary Figs. 13 and 14). Detailed SHINERS experimental procedures and validation of its non-perturbative nature in probing interfacial liquids were reported in our previous publications^{16,42}. The particle–HOPG gap regions (1–2 nm thick) are hotspots for plasmonic enhancement³². When immersed in aqueous solutions, these hotspots are filled by the interfacial liquid species, which contribute to the SHINERS signal^{19,31}. While bulk solution (more than ~ 2 nm away from the electrode surface) also gives rise to a small fraction of the Raman signal, its contribution was subtracted to obtain the SHINERS spectra presented in this work (Supplementary Figs. 15 and 16).

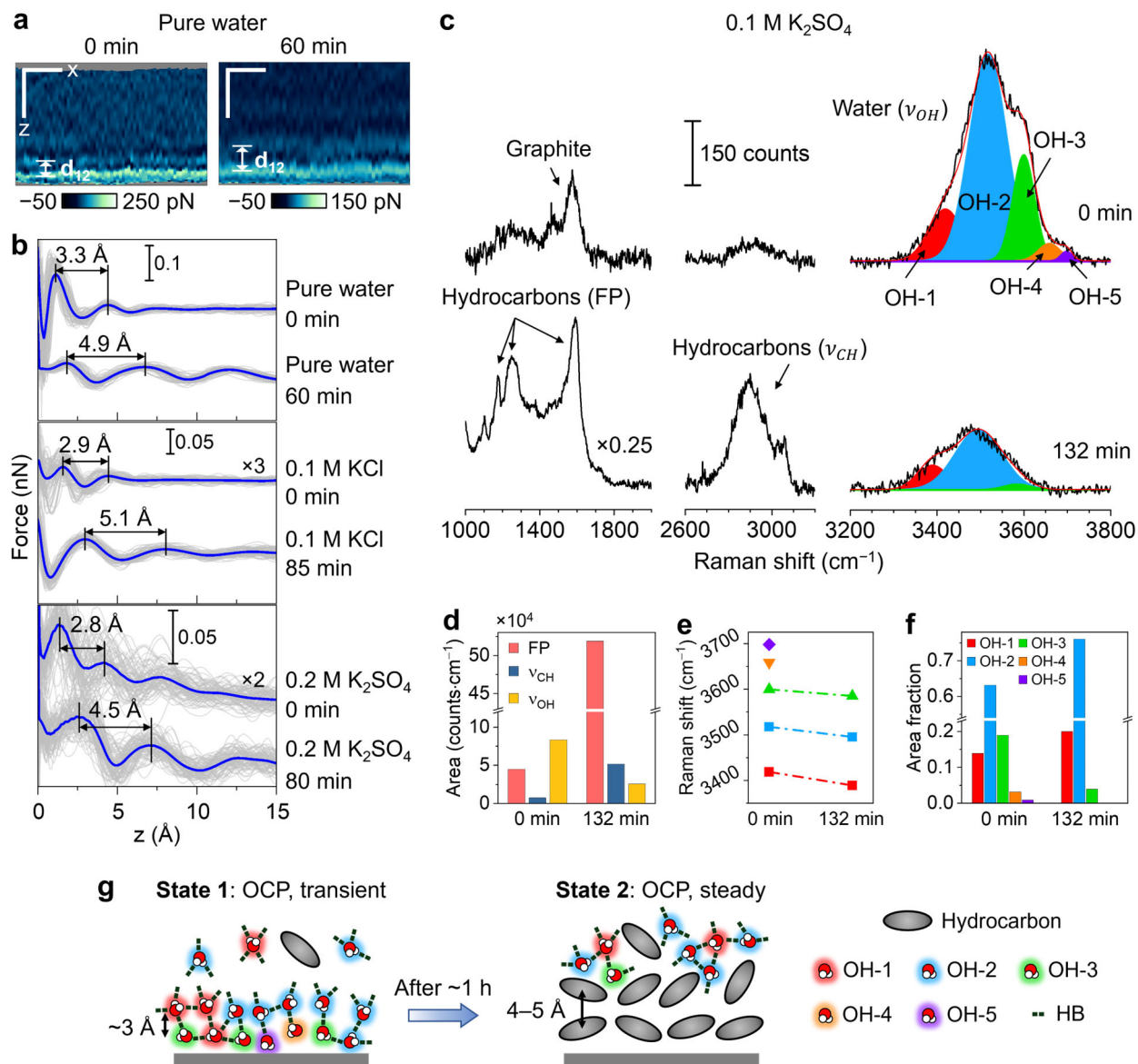


Fig. 2 | Time-dependent evolution of HOPG/aqueous solution interfaces at OCP. **a**, 3D-AFM x - z force maps of an HOPG/pure water interface obtained at the beginning of the measurement and after 60 minutes (conducted in Madrid). Scale bars: 1 nm. **b**, Force–distance curves of HOPG/pure water (top panel, extracted from **a**) and HOPG/aqueous solutions interfaces, at the beginning of the experiment and after 1–1.5 hours (Madrid). Individual curves are shown in gray, and average curves in blue. The interlayer distance d_{12} is marked on each set of curves. **c**, SHINERS spectra of an HOPG/0.1 M K₂SO₄ solution interface at the beginning ($t = 0$ min, top panel) and after 132 minutes (bottom panel). Left, middle, and right panels correspond to the fingerprint (FP), C–H stretching (v_{CH}), and O–H stretching (v_{OH}) modes, respectively. The v_{OH} band is deconvoluted into five individual Voigt peaks, OH-1 (red), OH-2 (blue), OH-3 (green), OH-4 (orange), and OH-5 (violet). **d**, Time evolution of the peak areas for FP, v_{CH} , and v_{OH} modes. **e, f**, Peak positions and area fractions of the individual v_{OH} peaks for $t = 0$ and 132 min. **g**, Schematic diagrams of the time-dependent evolution of HOPG–water interfaces at OCP, depicting the replacement of interfacial water by adventitious hydrocarbons and associated changes in the

hydrogen-bonding environment—specifically, an increase in the fractions of OH-1 and OH-2, a decrease in the fraction of OH-3 and the disappearance of OH-4 and OH-5 configurations.

The confocal Raman spectrum of bulk solution (0.1 M K₂SO₄ in water) confirmed the standard O–H stretching (ν_{OH}) band of water molecules between 3000–3700 cm⁻¹, as well as the absence of adventitious species within the sensitivity limit (Supplementary Fig. 15). In contrast, SHINERS spectra of an electrochemically cleaned HOPG–solution interface at OCP showed graphite G band^{43,44} at 1580 cm⁻¹, a weak C–H stretching (ν_{CH}) peak^{45,46} centered around 2900 cm⁻¹, and ν_{OH} band with a distinct shape compared to the bulk solution (Fig. 2c, top panels). The ν_{CH} mode can be attributed to the presence of small amounts of hydrocarbon species at the interface that may be either aliphatic or aromatic in nature^{47–49}. This unaged HOPG–solution interface can be viewed as “pristine”, since the amount of hydrocarbons inferred from the spectra is minute. The absence of hydrocarbons confirms the effectiveness of the electrochemical cleaning methods (details explained in the following sections) in removing the possible hydrocarbons at the original HOPG–solution interface and ligands on the Au/SiO₂ nanoparticle surface. After ageing for about 2 hours, the ν_{OH} band intensity became lower, ν_{CH} peaks became stronger, and a series of peaks emerged in the 1050–1700 cm⁻¹ range which we assign as different modes of hydrocarbon fingerprints (FP) (Fig. 2c, bottom panels). Possible origins of the FP modes include C–O stretches, C–F stretches, and aromatic ring vibrations, among others, although precise assignments are still under debate in the Raman community⁵⁰. The simultaneous decrease of water peaks (ν_{OH} peak area) and increase in hydrocarbon peaks (FP and ν_{CH} peak areas) (Fig. 2d) confirmed the interfacial accumulation of hydrocarbons that replaced the original hydration layers. This conclusion is consistent with the increase of interlayer distance from ~3 Å to 4–5 Å over time observed in the 3D-AFM results (Fig. 2a,b).

Remarkably, ageing leads to significant changes in the ν_{OH} peak components at the HOPG–solution interface. The ν_{OH} band at the pristine interface was decomposed into five peaks, OH-1–OH-5, with increasing peak positions at 3419, 3517, 3600, 3658, and 3698 cm⁻¹, respectively (Fig. 2c, top-right panel, and Fig. 2e). After ~2 hours of ageing, the first three peaks were red-shifted to 3389, 3495, and 3585 cm⁻¹, respectively, while the OH-4 and OH-5 peaks became absent or negligible (Fig. 2c, bottom-right panel, and Fig. 2e). For both pristine and aged interfaces, OH-2 remained the dominant peak, with area fractions of 63% and 76%, respectively; upon ageing, the OH-3 contribution significantly diminished (from 19% to 4%), while OH-1 became more prominent, increasing from 14% to 20% (Fig. 2f).

The assignment of ν_{OH} peaks, even for bulk water, remains controversial in modern literature, due to the complexity of the HB network of water (presence/absence of up to two donors and two acceptors for each water molecule) and the symmetry of the ν_{OH} vibration (symmetric vs antisymmetric)^{51–53}. Here we do not aim to precisely attribute each ν_{OH} peak to a specific HB configuration and/or vibrational symmetry, which would be practically unrealistic. Rather, we assign each peak to an approximate corresponding HB number (tetrahedral, trihedral, etc.) following existing interfacial water studies^{17,19,54,55}. Within one broad ν_{OH} spectrum, the typical consensus is that peak components with higher wavenumbers roughly correspond to lower HB coordination numbers^{17,19,54,55}.

Following the above approach, we attribute OH-1 to an HB number close to 4 (either 4-fold or a combination of 4-fold and 3-fold coordination), and OH-2 to an HB number near 3 (either 3-fold or a combination of 3-fold and 2-fold coordination)^{19,54–58}. The assignments for OH-3 to OH-5 will be discussed later. In comparison, bulk aqueous solution only has two ν_{OH} peak components, OH-1 and OH-2 (Supplementary Fig. 15). Compared to the bulk solution, the pristine HOPG–solution interface features a much smaller fraction of OH-1, slightly larger OH-2, and the emergence of OH-3 to OH-5, indicating strong HB breaking effects. After ageing, the overall HB number of water at the HOPG–solution interface became higher, as evidenced by the increased area fractions of OH-1 and OH-2 and decreased fractions or absence of OH-3 to OH-5. This reveals that the hydrocarbon layers are less effective in breaking HBs of nearby water compared to HOPG. The red shift of the peaks after ageing, on the other hand, is likely due to the weaker hydrophobic interaction between water molecules and the dynamically moving, less dense hydrocarbon layers (aged interface) compared to the fixed, densely packed HOPG substrate (pristine interface).

In SHINERS measurements, the active interfacial liquid regions contributing to the signal are sandwiched between the HOPG surface and SiO₂ (shell of the Au/SiO₂ particles) (Fig. 1d). To rule out the possible role of silica in producing the emergent interfacial ν_{OH} peaks (OH-3 to OH-5), we designed and fabricated a control sample, Au film/SiO₂/electrolyte/SiO₂/Au nanoparticles. As shown in Supplementary Fig. 17, the silica layer is ~ 3 nm thick at the active gap region. This sample serves as a well-defined control system that enables Raman enhancement, is graphite-free, and ensures SiO₂ is the dominant surface composition in contact with the probed volume of aqueous solution. SHINERS spectra of this control sample at multiple different areas and varying electrode potentials did not exhibit OH-3 to OH-5 peaks (Supplementary Fig. 17), distinct from the results obtained for HOPG/solution interfaces. These data prove that the silica shell layer does not directly contribute to the SHINERS peaks of the HOPG–water interface.

Combining 3D-AFM and SHINERS results, we propose the overall structure of the HOPG–water interface at OCP, as summarized in Fig. 2g. A clean, unaged interface is in State 1, featuring multiple (at least 2–3) water layers separated by ~ 3 Å. The interfacial water has strongly broken HBs compared to bulk water and a diverse distribution of HB configurations. After ageing, the interface evolves into State 2, which is dominated by 2–3 layers of hydrocarbon molecules with 4–5 Å separation. Water is mostly depleted from the hydrocarbon layers. The water molecules above the hydrocarbons have overall higher HB coordination numbers than those at pristine HOPG surfaces, yet still lower than that of bulk water.

Electrified graphite–water interfaces: pristine response

After identifying the two distinct states of the HOPG–water interfacial structure, we proceeded to investigate their potential dependence. As is common for graphite and metallic electrodes, positive potentials tend to induce surface oxidation^{19,59,60}. Therefore, to preserve the electrode structure and to enable the generalization to a broad range of electrode–water interface systems, we applied negative potentials to the HOPG electrode. The potential range was typically ~ 0 V to -2.2 V vs Ag/AgCl, large enough to examine rich reconfiguration effects of the interfacial structure. At sufficiently negative potentials, hydrogen evolution reaction (HER) became significant (Supplementary Fig. 18), producing bubbles in the local area that prevented further 3D-AFM and SHINERS measurements. The bubble onset potential varied for different samples and local areas, but it remained in the -1.6 V to -2.6 V range (vs Ag/AgCl).

In previous microscopy or spectroscopy studies of electrified solid–water interfaces, there was a lack of control of the initial interfacial configuration at OCP, as the system could be in either State 1 or State 2, or an intermediate regime^{12,18–20,28,61}. This is likely the key reason why existing literatures show significant discrepancies regarding the effect of electrode potential/electric field on the interfacial water configuration (Supplementary Tables 1–4). To resolve such controversies, here we first prepared the HOPG–aqueous solution system to State 1, before examining the potential dependence. State 1 was achieved by either limiting the total sample preparation/air exposure time to no more than a few minutes before starting the measurement, or via electrochemical cleaning after the sample was prepared (as discussed later). State 1 was confirmed when d_{12} was observed to be ~ 3 Å in 3D-AFM, or when FP and v_{CH} peaks were either negligible or much weaker than the v_{OH} peak in SHINERS.

We first performed potential-dependent 3D-AFM in a series of aqueous solutions containing either K_2SO_4 (0.01–0.2 M) or KCl (0.1 M). A total set of 9 independent 3D-AFM measurements were conducted with a starting condition of $d_{12} \sim 3$ Å (State 1) at OCP, as shown in Fig. 3a,b and Supplementary Figs. 3–9. To minimize the possible convolution of ageing to the potential-dependence of the interfacial water structure, the measurements were conducted either quickly (within ~ 20 minutes for each potential scan) to mitigate ageing or in an argon-sealed liquid cell to slow down the ageing process. All of the obtained force curves, regardless of the measurement location (Urbana or Madrid) and environmental condition, revealed that d_{12} is remarkably potential independent within at least 0 to -2.2 V vs Ag/AgCl. While each individual set of 3D-AFM results showed small variations of d_{12} mostly within 3.0–3.5 Å, the overall average values were always near 3.3 Å at each of the applied potentials (Fig. 3b).

The observed potential-independence of interlayer distance might seem counterintuitive, since potential modulations are typically expected to induce changes in the ionic concentration at the interface. However, for dilute aqueous solutions (< 1 M) at solid interfaces, a large body of publications supported the salt concentration-independence of the ~ 3 Å hydration layer spacing^{9,11,30,38,39}. Applying an electrode potential is nearly equivalent to modulating the interfacial ionic concentration, and the solutions with different concentration also exhibited similar d_{12} in our results. This is likely because water is still the dominant species within the first 1–2 nm from the HOPG surface in the potential range we studied.

Although the interlayer spacing is potential-independent, the polar water molecules at the interface are expected to change their orientations and thus the HB configurations at different electric fields. We investigated such effects through multiple sets of SHINERS measurements (Fig. 3c and Supplementary Figs. 19 and 20). Similar to 3D-AFM measurements, we first prepared the samples to reach State 1 at OCP, as evident from the weak or negligible FP and v_{CH} peaks. As shown in Fig. 3c, the hydrocarbon-related modes were absent not only at OCP, but also throughout all the applied potentials, confirming that the interface remained pristine during the whole measurement process. The v_{OH} mode consistently exhibited five peak components across all applied potentials. At more negative potentials, the overall v_{OH} band became broader while the height decreased. The total area of v_{OH} remained nearly constant (Fig. 3d), again confirming that the total amount of interfacial water molecules was potential-independent within the sensitivity limit. This is consistent with the potential-independent force curves and d_{12} in the 3D-AFM results (Fig. 3a,b).

Since water molecules are neutral yet polar, an interfacial electric field can induce the reorientation of the molecules without changing their average distance from the electrode surface, thus preserving the d_{12} and average interfacial density.

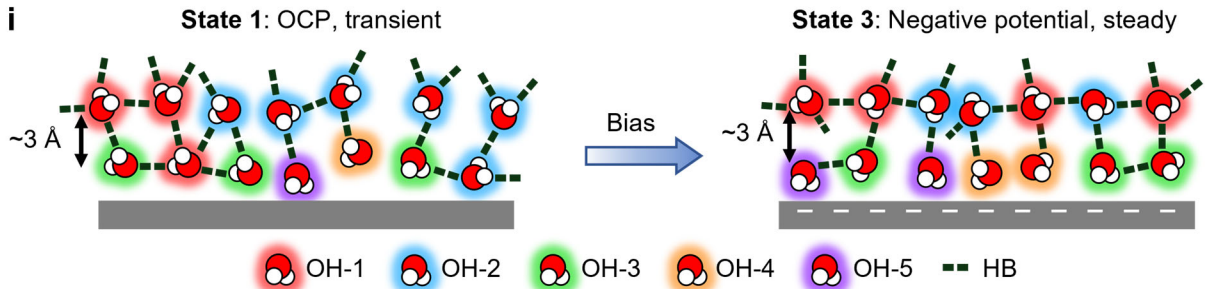
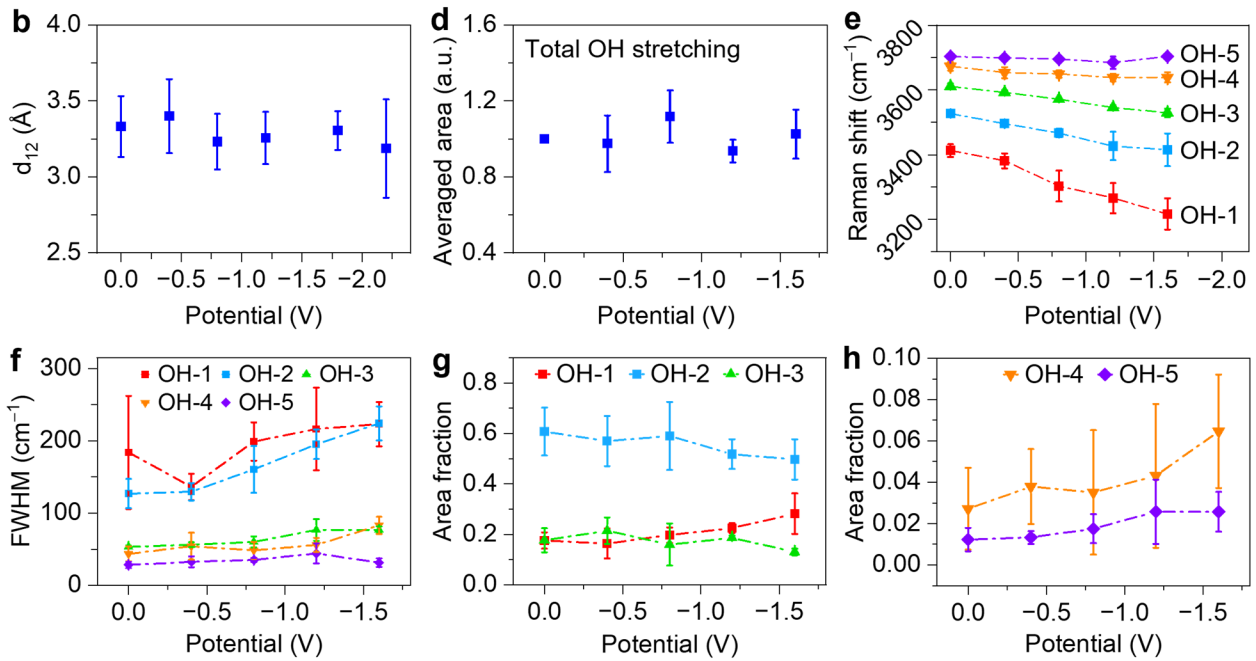
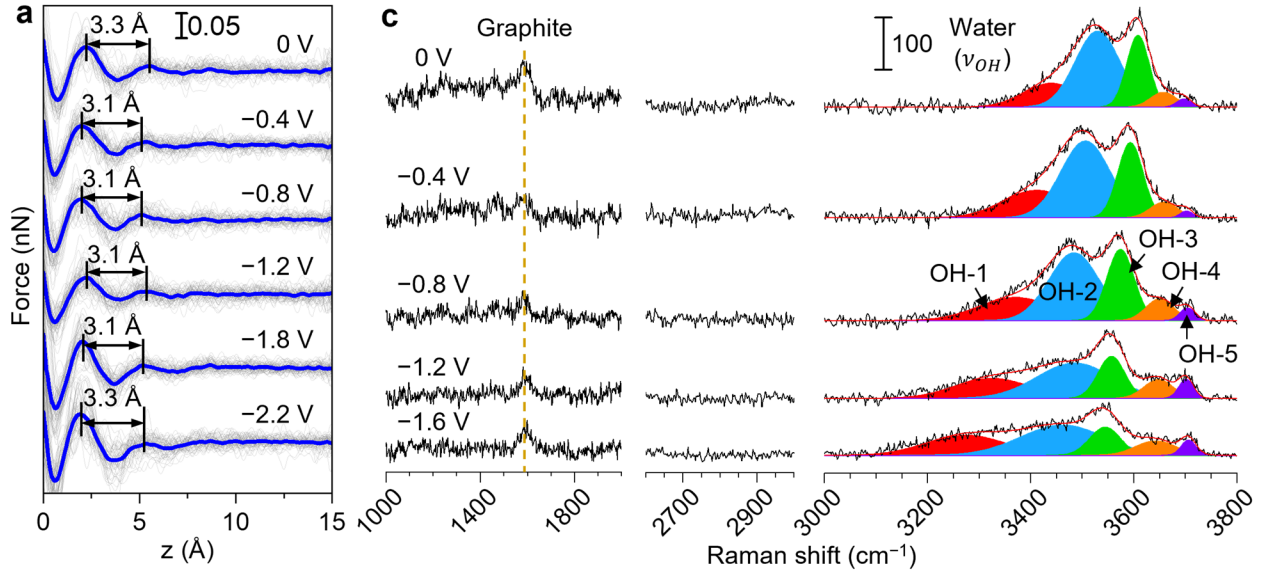


Fig. 3 | Effect of electrode potential on pristine HOPG/aqueous solution interfaces. **a**, Force–distance curves extracted from 3D-AFM maps of a pristine HOPG/0.01 M K₂SO₄ aqueous solution interface at different potentials vs Ag/AgCl (Urbana). Gray: average curves of single x–z maps, blue: average of the gray curves. d_{12} is marked on each curve. **b**, Average values of d_{12} as a function of the electrode potential. Data were obtained from several experimental runs (multiple potential scans in each experiment) including the ones depicted in **(a)** and Supplementary Figs. 3–8. **c**, SHINERS spectra of a pristine HOPG/0.1 M K₂SO₄ aqueous solution interface at a series of electrode potentials vs Ag/AgCl (Urbana). The ν_{OH} mode is deconvoluted into 5 Voigt peaks, OH-1 to OH-5. **d–h**, Key SHINERS metrics of pristine HOPG/0.1 M K₂SO₄ solution interface as a function of electrode potential. Data were extracted from SHINERS results in **(c)** and Supplementary Figs. 19 and 20. The metrics include **(d)** the averaged total area of the ν_{OH} peak (before averaging, peak areas were normalized by scaling the area of the 0 V data to 1 for each potential scan), **(e)** Raman shift (peak position) of OH-1 to OH-5, **(f)** Full width at half maximum (FWHM) of OH-1 to OH-5, **(g)** area fractions of OH-1 to OH-3 (ratio of each peak versus the total area of the ν_{OH} mode), and **(h)** area fraction of OH-4 and OH-5. **i**, Schematic representation of the potential-driven transition of a pristine graphite–water interface from State 1 to State 3, illustrating the key observations: constant d_{12} , constant amounts of interfacial water, and HB diversification (less OH-2 and more OH-1, OH-4, and OH-5) at negative potentials.

We further analyzed the potential-dependence of the individual ν_{OH} peaks (OH-1 to OH-5). OH-1 to OH-4 exhibited red-shifts at more negative potentials (Fig. 3e), likely due to Stark effects. In contrast, OH-5 remained at the same position ($\sim 3700\text{ cm}^{-1}$) at different potentials. The width of all the peaks exhibited certain levels of increase at more negative potentials (Fig. 3f), leading to an overall broadening of the ν_{OH} band. Among the five peaks, OH-2 showed the most pronounced increase in peak width. The broadening effects are likely due to the larger variations in the HB configurations that contribute to each peak, as a result of the interfacial electric field. For example, the OH-2 peak may consist of at least two configurations, one with two donors and one acceptor (DDA), the other with one donor and two acceptors (DAA)^{17,56}. At a stronger electric field, the difference in the vibrational energy of these two configurations may become larger; in addition, each configuration may be further split into sub-configurations with different vibrational energies resulting from their orientational differences (e.g., parallel vs vertical to the electric field). These effects can lead to a broadening of the OH-2 peak. We further observed that the area fraction of OH-2 decreased, OH-3 nearly constant, and OH-1, OH-4, and OH-5 increased at more negative potentials (Fig. 3g,h). The evolution in area fractions also signifies the diversification of HB configurations, where some OH-2 structures split into configurations with either larger (OH-1) or smaller (OH-3 to OH-5) HB numbers, due to the orientation-dependent free energy modulations induced by the interfacial electric field.

The higher-wavenumber peaks, OH-3 to OH-5, are expected to correspond to configurations with low HB numbers, such as 2-coordinated water, cation-coordinated water, dangling O-H, and nondonor (ND) water, although the exact peak assignments remain highly controversial^{17,19,54–58}. Nevertheless, one special property worth noting is the lack of Stark shift of OH-5 over the large range of potentials, which was consistently observed in each of the 7 potential scans over 3 independent sets of measurements where OH-5 was present (Figs. 3c,e and Supplementary Figs. 19–22). The Stark shift at a given electric field, to the first order approximation, is proportional to

the difference in the dipole moment between the ground and excited state along the direction of the electric field^{62,63}. Therefore, the OH-5 configuration likely has a nearly fixed molecular orientation (no significant fluctuation over time) with a difference dipole parallel to the substrate surface (perpendicular to the interfacial electric field), thus having zero Stark effect. Among all the reported weakly coordinated HB configurations, to the best of our knowledge, there is only one possible state fulfilling this criterium—the antisymmetric OH stretching of ND water. The ND configuration, proposed before in a previous study of Au–water interface¹⁸, may exist at the first hydration layer with oxygen pointing up and two hydrogen atoms down (in close proximity to the substrate). While the ground state dipole moment is vertical, the difference dipole of the antisymmetric OH stretching is parallel to the substrate, resulting in zero Stark shift. We thus assign OH-5 to the antisymmetric v_{OH} of ND water.

Figure 3i illustrates the overall potential-dependent response of the pristine HOPG–water interface, combining results from 3D-AFM and SHINERS. At negative potentials, the originally transient State 1 evolves into a steady State 3. In this process, the interface remains water-dominated, with constant ~ 3 Å hydration layer spacing and the same overall interfacial water density. The HB configurations of the interfacial water become more diverse, featuring a simultaneous increase of both the “ice-like” 4-coordinated structures and a few low-coordinated states including the “monomer-like” or “gas-like” ND water.

Electrified graphite–water interfaces: non-pristine response

We further investigated the influence of negative potentials on the initially non-pristine HOPG–water interface. State 2, featuring $d_{12} \sim 4\text{--}5$ Å or FP (or v_{CH}) peak intensity higher than that of v_{OH} , was reached either unintentionally right after sample preparation (due to adventitious airborne or liquid-borne hydrocarbons), or intentionally through >1 hour ageing under ambient conditions after HOPG surface was immersed in the aqueous solution.

Starting from State 2, we conducted a series of 6 potential-dependent 3D-AFM experiments (Urbana and Madrid), with K_2SO_4 in water (0.01–0.2 M) and KCl in water (0.1 M) as the electrolyte (Fig. 4a,b and Supplementary Figs. 10 and 11). All results consistently showed an abrupt decrease of d_{12} from 4–5 Å to ~ 3 Å at negative potentials, where the transition mostly occurred between -1 V to -1.5 V vs Ag/AgCl. After the transition, further decrease of the electrode potential did not induce more changes in d_{12} , which remained at ~ 3 Å in all the data sets (Fig. 4a,b and Supplementary Figs. 10 and 11). These results suggested that the hydrocarbons were removed from the interface and replaced by water molecules at sufficiently negative potentials, and the water-dominated interfacial configuration was stable under the negative polarization conditions.

Right after the potential was changed back to OCP, the force curves remained mostly unchanged, with the same ~ 3 Å interlayer distance (Fig. 4a,b and Supplementary Figs. 4, 5, 11a, and 12). However, after about 1 to 2 hours under OCP condition, with the aqueous solution exposed to ambient air, we observed a transition of d_{12} back to $\sim 4\text{--}5$ Å (Supplementary Fig. 12). These results are consistent with the ageing effects shown in Fig. 2, confirming that the system reached the transient State 1 right after the potential was switched from negative to OCP, before evolving into the steady State 2 over time under OCP.

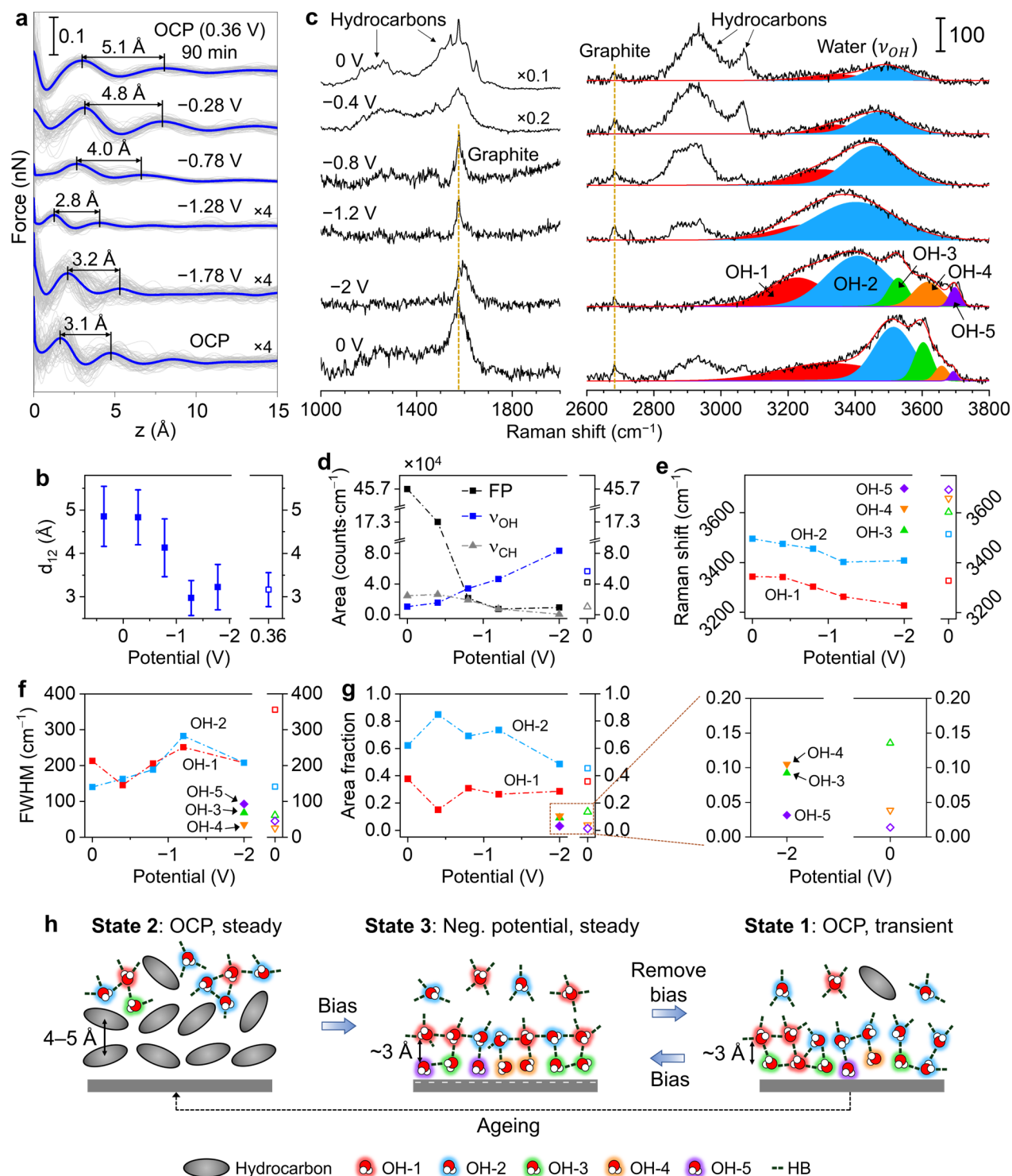


Fig. 4 | Influence of the electrode potential on non-pristine HOPG/aqueous solution interfaces. **a**, Force–distance curves extracted from 3D-AFM maps of an initially non-pristine HOPG/0.1 M KCl in water interface at a series of electrode potentials (Madrid). Gray: individual force–distance curves; blue: averaged curve. d_{12} is marked on each curve. Before starting the measurements, the HOPG surface was immersed in the 0.1 M KCl solution surrounded by ambient air for 90 minutes to reach a non-pristine state (State 2). The sequence of electrode potentials

proceeded as OCP (0.36 V), -0.28 V, -0.78 V, -1.28 V, -1.78 V (vs Ag/AgCl) and OCP. **b**, d_{12} extracted from **(a)** and plotted as a function of the electrode potential. **c**, SHINERS spectra of a non-pristine HOPG/0.1 M K_2SO_4 in water interface at different electrode potentials (Urbana). Before measurements, the electrochemical cell was exposed to ambient air for ~ 270 minutes to reach a non-pristine state (State 2). The sequence of potentials proceeded as 0 V, -0.4 V, -0.8 V, -1.2 V, -2 V and 0 V (vs Ag/AgCl). **d–g**, Key SHINERS metrics of the initially non-pristine HOPG/0.1 M K_2SO_4 solution interface as a function of electrode potential. Data were extracted from results in **(c)**. The obtained metrics include **(d)** area under the FP, v_{CH} and v_{OH} peaks, and **(e)** Raman shift (peak position), **(f)** FWHM and **(g)** area fraction (ratio of each peak vs the total area of the v_{OH} mode) for OH-1 to OH-5. **h**, Schematic representations of the overall HOPG–water interfacial structural transitions due to ageing and electrode potential.

We also conducted a series of potential-dependent SHINERS measurements for HOPG/0.1 M K_2SO_4 in water starting from State 2, with results summarized in Fig. 4c and Supplementary Figs. 21–23. In all of these results, FP and v_{CH} bands were much stronger than that of the v_{OH} at initial OCP or 0 V (vs Ag/AgCl) condition, consistent with the State 2. At negative potentials, the hydrocarbon FP and v_{CH} bands became weaker and eventually negligible at ~ -1 V to -2 V vs Ag/AgCl (Fig. 4c,d and Supplementary Figs. 21–23). In contrast, the overall intensity of v_{OH} became stronger. After the potential was gradually changed back to 0 V (ramping from -2 V to 0 V in ~ 1 hour), the hydrocarbon-related peaks only slightly recovered, while the overall intensity/area of v_{OH} was largely preserved (Fig. 4c,d and Supplementary Figs. 21 and 22). These results further confirmed the transition from hydrocarbon to water at the HOPG–aqueous solution interface at negative potentials (State 2 to State 3), as well as the reversal to the pristine State 1 immediately after the removal of the electrode potential.

After decomposing the v_{OH} band, we identified up to two peaks, OH-1 and OH-2, within the ~ 0 to -1.2 V (vs Ag/AgCl) potential range (Fig. 4c and Supplementary Figs. 21b, 22b, and 23b). In this regime, at more negative potentials, the two peaks red-shifted due to the Stark effect and became wider (Fig. 4e,f). These observations are remarkably consistent with the potential-induced v_{OH} peak component evolutions of the initially pristine interface (Fig. 3c–h), revealing that the water surrounding the hydrocarbon layers also exhibit HB diversification effects with increasing interfacial electric field. We further observed that the area fractions of OH-1 and OH-2 remained mostly constant (Fig. 4g, 0 to -1.2 V), indicating that the average HB number did not change within this potential range. As the potential reached -2 V, the OH-3 to OH-5 components suddenly emerged, at the same time when the hydrocarbon-related peaks nearly completely disappeared (Fig. 4c). This transition, together with the ageing effect shown in Fig. 2c, reveals that direct contact between water and the graphite surface is a prerequisite for the formation of the low-coordination OH-3 to OH-5 configurations. The interfacial electric field, on the other hand, only modulates the dispersion within the existing modes without introducing emergent HB configurations. Additionally, at -2 V, the peak position, FWHM, and area fractions of OH-1 to OH-5 (Fig. 4e–g) are mostly consistent with those of the initially pristine system at high negative potentials (Fig. 3e–h), further confirming that the same pristine State 3 was reached in both cases.

As the potential returned to 0 V, nearly all the features of OH-1 to OH-5 were restored to those characteristic of the pristine State 1 (compare the final 0 V data in Fig. 4e–g to the initial 0 V data

in Figs. 3e–h). Note that small hydrocarbon FP and ν_{CH} bands emerged at the final 0 V state (Fig. 4c). This was due to the gradual change of potential from -2 V to 0 V (see Supplementary Fig. 21c,d) that took ~ 1 hour, during which small amounts of hydrocarbons accumulated at the interface. Nevertheless, the interface was still dominated by water at the final 0 V state and the ν_{OH} modes remained similar to those of the ideal pristine states.

The overall structural transitions among all the three observed states of the HOPG–water interface are summarized in Fig. 4h. Despite the distinct interfacial structures in State 1 and State 2, they converge to the same State 3 under sufficiently negative electrode potentials. We propose two possible origins of this effect. One is the change of the interfacial free energy. Since water is polar while hydrocarbons are nonpolar, an interfacial electric field will lower the enthalpy of water molecules with the alignment of the dipoles to the field, while the hydrocarbons' free energy is not affected. When the electrostatic free energy modulation of the water dipoles is sufficiently large, it may overcome the interaction energy between the hydrocarbons and graphite surface, resulting in the swapping between water and hydrocarbons at the interface. Simplified calculations show that this scenario is plausible (Supplementary Note 1). The other possibility is electrochemical reactions, including hydrogen evolution and direct hydrocarbon reduction. Cyclic voltammetry measurements revealed hydrogen evolution in the measured potential range (Supplementary Fig. 18), which can produce hydrogen bubbles that may propel the hydrocarbons away from the electrode surface. Additionally, direct electroreduction of hydrocarbons which contain C–O, C–F and aromatic rings is also possible^{64–66}.

Conclusion and outlook

We have resolved the long-standing controversy on the structure of graphite–water interfaces. By combining microscopy and spectroscopy methods, and precisely controlling the initial sample preparation, ageing time, and electrode potential, we identified the hitherto hidden co-existence of three interfacial states. At open circuit or a nearly neutral surface, the interface can be in either the pristine, water-dominant state, or the non-pristine, hydrocarbon-dominant state. At sufficiently negative potentials, the interface inevitably transitions into a pristine state with a diverse distribution of hydrogen bond configurations, including monomer-like non-donor water. The hydrogen bond configurations at the interface are subject to modulations of three factors: the graphite surface, the hydrocarbon layer, and the interfacial electric field. We have distinguished the contribution of each factor, and constructed a universal interfacial configuration diagram under varying surface charge and ageing conditions.

We expect the results to be applicable to not only graphite, but also a large range of other solid–water interfaces. Except for a few model systems, such as freshly cleaved mica or calcite, most real-life and industrially relevant solids (e.g., most semiconductors and metals) exhibit certain levels of hydrophobicity^{67–69}. Oftentimes, these surfaces become more hydrophobic upon air exposure, due to the accumulation of hydrocarbons or other airborne species^{67–69}. We anticipate that these solid–water interfaces will also exhibit multiple interfacial states, which are subject to ageing in ambient environments and to electric field-driven transitions from non-pristine to pristine states, accompanied by strong hydrogen bond reconfigurations of the interfacial water.

The ability to identify the realistic structure of solid–water interfaces and deconvolute the contributing factors will be crucial for the rational design of relevant systems for practical

applications, such as electrochemical energy conversion and storage, biosensing, and photocatalysis.

Methods

Materials

ZYB grade highly oriented pyrolytic graphite (HOPG) was obtained from Bruker Corporation.

Madrid: Potassium sulfate (K_2SO_4 anhydrous, 99+%, Sigma-Aldrich) or potassium chloride ($\geq 99.0\%$, Sigma-Aldrich) and ultrapure water (ELGA Maxima, $18.2 M\Omega \cdot cm$) were used for preparing electrolyte solutions of various concentrations. Glass vials were rinsed with acetone ($\geq 97.0\%$, Sigma-Aldrich), isopropanol (99.6%, Acros Organics) and ultrapure water before preparing the electrolyte solutions.

Urbana: Potassium sulfate (K_2SO_4 anhydrous, 99+%, Acros Organics) and ultrapure water ($18.2 M\Omega \cdot cm$; Synergy UV system, Millipore Sigma) were used for preparing electrolyte solutions of various concentrations. Glass vials were rinsed with acetone, isopropanol, and ultrapure water, and in some cases, flame-annealed before being used to prepare electrolyte solutions.

3D-AFM

3D-AFM measurements were independently performed in Madrid (Spain) and Urbana (IL, USA) using amplitude modulation mode with similar methodologies. In both cases, the cantilever was photothermally excited at its first resonance frequency. A low frequency sinusoidal signal (10–100 Hz) was applied to the z-piezo to modulate the tip–sample distance, synchronized with the x-displacement, to ensure a full z-cycle at each x-position. Amplitude and phase signals were recorded as functions of x, y and z. We found that the signal obtained over x–z frames and 3D volumes tends to better represent the overall interfacial structure compared to a series force–distance curve obtained at a fixed (x, y) point. The latter approach is sensitive to the local variations of the substrate surface, such as the lattice sites, impurities, adventitious adsorbates, etc., and are thus less representative of the overall interfacial liquid configuration.

In Madrid, measurements were performed using a Cypher S system (Asylum Research Inc., USA) with custom-developed 3D-AFM software. In Urbana, a Cypher ES system (Asylum Research Inc., USA) with the AC Fast Force Mapping (AC FFM) module was used. Silicon probes were used for the 3D-AFM measurements: Arrow-UHFAuD (NanoAndMore, Germany) in Madrid, and FS-1500AuD (Asylum Research) and PPP-NCHAuD (Nanosensors) in Urbana. Cantilever calibration was performed using the contactless Sader method, as implemented in the commercial AFM software as *GetReal*.

Cantilevers were cleaned using sequential solvent-rinsing followed by UV-ozone treatment. In Madrid, cantilevers were immersed in a mixture (50:50 in volume) of isopropanol (99.6%, Acros Organics) and ultrapure water, then thoroughly rinsed with ultrapure water. In Urbana, cantilevers were sequentially soaked in acetone (~30 minutes), isopropanol (~12 hours) and ultrapure water (~1 hour), then dried using ultra-high purity argon (6N, Airgas) or a compressed air duster (Office Depot). After drying, UV-ozone treatment was applied. In Madrid, cantilevers were exposed for ~1 hour using a PSD-UV3 system (Novascan Technologies, USA). In Urbana, ~5-minute exposure

was performed using a ProCleaner Plus system (BioForce Nanosciences), with the AFM probe positioned ~5 cm from the UV source.

Additional details on the cantilever calibration values and 3D-AFM parameters are summarized in Supplementary Tables 5–8.

Electrode potential control was implemented using either a three-electrode or a two-electrode configuration (shown in Supplementary Fig. 24)^{16,70–72}. In both lab setups, freshly cleaved HOPG was used as the working electrode and platinum served as both a quasi-reference and counter electrodes. In the Madrid lab, a three-electrode setup was used with platinum foils (0.1 mm thick, 99.99+%, Sigma-Aldrich) connected to a PalmSens4 potentiostat (PalmSens). The platinum foils were cleaned using piranha solution (2:1 H₂SO₄:H₂O₂), followed by sonication in ultrapure water for 5 minutes. In the Urbana lab, a two-electrode setup was employed, using a platinum ring as the combined counter and quasi-reference electrode. The ring was cleaned by sequential rinsing in acetone, isopropanol and ultrapure water, followed by drying with argon or a compressed air duster. Electrode potential was applied and monitored using a Keithley 2450 source meter. Urbana's Cypher ES featured environmental control of the cell chamber, which was purged with argon for ~1–2 minutes and tightly sealed, enabling stable operation over at least 2 days without any noticeable change in liquid volume.

All measurements were performed at room temperature and pressure.

3D-AFM data processing

Established force reconstruction methods^{73,74} were implemented using custom-written codes to reconstruct the conservative component of the AFM probe–sample interaction force. To enhance the force signal and improve the visualization of interfacial layers, the Madrid lab applied binomial smoothing (range = 2) followed by background subtraction using a single-exponential fit, while the Urbana lab employed a 50-point moving average and a double-exponential background subtraction.

In the Madrid lab's workflow, a single representative *x*–*z* map was selected from each 3D-AFM data set and analyzed in detail by examining the individual force–distance curves and their average. The substrate position (*z* = 0) was defined based on the setpoint amplitude. The Urbana lab averaged each *x*–*z* map within a 3D-AFM set into a single force–distance curve. Prior to averaging, the force–distance curves were aligned based on the tip–sample separation corresponding to a phase shift of 22 degrees below the free oscillation phase. The substrate position (*z* = 0) was then defined as the *z*-position (below the first water layer) where the force value equaled that at the first water layer position, following previously reported protocols⁶. The *x*–*z* map-averaged force–distance curves were then collectively analyzed, and their overall histogram and average were used to represent the interfacial structure of the entire 3D volume.

Raman spectroscopy

Raman spectroscopy experiments were performed at Urbana. All Raman measurements were carried out on a confocal Raman imaging system (Horiba, LabRAM HR 3D-capable Raman spectroscopy) with a 633 nm excitation laser at 3.5 mW power. The beam was focused onto the sample surface using either a 50× (with numerical aperture (NA) of 0.5) or 10× (NA 0.25) objective. Scattered light passed through a 300 grooves/mm grating and was directed to a Horiba Synapse back-illuminated deep-depletion charge-coupled device (CCD) camera. Raman

spectra from 300 cm^{-1} to 4000 cm^{-1} were collected with an accumulation time of 20–30 seconds, and repeated 3–6 times for averaging unless otherwise specified. A silicon wafer was used for spectral calibration at the beginning or end of the experiment.

A Raman spectrum of bulk $0.1\text{ M K}_2\text{SO}_4$ aqueous solution (Supplementary Fig. 15) was obtained with laser focused on a HOPG surface in the absence of Au/SiO₂ core/shell nanoparticles. A 50× objective (NA 0.5) and an acquisition time of 20 seconds with 6 accumulations were used.

The preparation of Au/SiO₂ core/shell particles was described elsewhere⁴² and is briefly explained here. A 10 ml 0.01 wt.% HAuCl₄ ($\geq 99.9\%$, Sigma Aldrich) aqueous solution was first heated to boiling, then 0.07 ml of 1 wt.% sodium citrate aqueous solution ($>99\%$, Alfa Aesar) was added into the boiling solution and kept heated for 30 minutes. The resulting solution was cooled to room temperature and characterized by UV-vis spectrophotometer. A characteristic absorption peak at $\sim 534\text{ nm}$ indicated the formation of $\sim 60\text{ nm}$ Au nanoparticles (Supplementary Fig. 13a). For silica coating, 3 ml of the synthesized bare Au particles solution, together with 0.04 ml 1 mM APTMS solution (Sigma Aldrich) and 0.32 ml 0.54 wt.% sodium silicate solution (Sigma Aldrich), were heated to $90\text{ }^\circ\text{C}$ and kept for 2 hours. The solution was then cooled in an ice bath. To remove ligands and other by-products, 3 ml of the as-synthesized particles were centrifuged at $2020 \times g$, 10 minutes. After discarding the supernatant, the particles were re-dispersed in 1.5–3 ml of ultrapure water. This centrifugation and supernatant removal process was repeated up to five times, and the final product was dispersed in 200 μl of ultrapure water. Transmission electron microscopy (TEM) verified the morphology of the Au/SiO₂ particles, while cyclic voltammetry confirmed if the silica shell is pin-hole free (Supplementary Fig. 13b,c).

SHINERS measurements were performed using either a commercial EC cell purchased from DEK Research Instrumentation (Supplementary Fig. 24d) or a similar home-made cell. The as-prepared Au/SiO₂ core/shell particle solution was drop-casted onto the freshly cleaved HOPG surface and dried in air for 1–2 hours. This often resulted in non-uniform particle distribution, forming coffee ring-like structures. SHINERS spectra were typically collected ~ 20 – 30 microns from the coffee ring's edge. A sub-monolayer coverage is expected in these areas (Supplementary Fig. 14). An Ag/AgCl reference electrode (BaSi, 3M NaCl, MF-2052) and a Pt wire counter electrode (CH Instrument, CHI115) were used in the SHINERS measurements.

All measurements were performed at room temperature and pressure.

Electrode potential calibration

All the results in this work are reported against Ag/AgCl, unless otherwise specified. The potential difference between the Pt quasi-reference and a standard Ag/AgCl reference electrode (BaSi, 3 M NaCl, MF-2052) was obtained by comparing the corresponding equilibrium redox potential of the redox couple Ferri/Ferrocyanide (5 mM) in $0.1\text{ M K}_2\text{SO}_4$ solution. The potential against Pt was found to be 0.22 V vs Ag/AgCl (Supplementary Fig. 25).

References

1. Björneholm, O. *et al.* Water at Interfaces. *Chem. Rev.* **116**, 7698–7726 (2016).

2. Mondal, J. A., Nihonyanagi, S., Yamaguchi, S. & Tahara, T. Structure and Orientation of Water at Charged Lipid Monolayer/Water Interfaces Probed by Heterodyne-Detected Vibrational Sum Frequency Generation Spectroscopy. *J. Am. Chem. Soc.* **132**, 10656–10657 (2010).
3. Pham, T. A., Ping, Y. & Galli, G. Modelling heterogeneous interfaces for solar water splitting. *Nat. Mater.* **16**, 401 (2017).
4. Wang, T. *et al.* Enhancing oxygen reduction electrocatalysis by tuning interfacial hydrogen bonds. *Nat. Catal.* **4**, 753–762 (2021).
5. Omta, A. W., Kropman, M. F., Woutersen, S. & Bakker, H. J. Negligible Effect of Ions on the Hydrogen-Bond Structure in Liquid Water. *Science* **301**, 347–349 (2003).
6. Uhlig, M. R., Martin-Jimenez, D. & Garcia, R. Atomic-scale mapping of hydrophobic layers on graphene and few-layer MoS₂ and WSe₂ in water. *Nat. Commun.* **10**, 2606 (2019).
7. Seibert, S., Klassen, S., Latus, A., Bechstein, R. & Kühnle, A. Origin of Ubiquitous Stripes at the Graphite–Water Interface. *Langmuir* **36**, 7789–7794 (2020).
8. Lucky, C. & Schreier, M. Mind the Interface: The Role of Adsorption in Electrocatalysis. *ACS Nano* **18**, 6008–6015 (2024).
9. Martin-Jimenez, D., Chacon, E., Tarazona, P. & Garcia, R. Atomically resolved three-dimensional structures of electrolyte aqueous solutions near a solid surface. *Nat. Commun.* **7**, 12164 (2016).
10. Miyazawa, K. *et al.* A relationship between three-dimensional surface hydration structures and force distribution measured by atomic force microscopy. *Nanoscale* **8**, 7334–7342 (2016).
11. Umeda, K. *et al.* Atomic-resolution three-dimensional hydration structures on a heterogeneously charged surface. *Nat. Commun.* **8**, 2111 (2017).
12. Tang, Z., Lin, S. & Wang, Z. L. Unveiling Contact-Electrification Effect on Interfacial Water Oscillation. *Adv. Mater.* **36**, 2407507 (2024).
13. Nakouzi, E. *et al.* Moving beyond the Solvent-Tip Approximation to Determine Site-Specific Variations of Interfacial Water Structure through 3D Force Microscopy. *J. Phys. Chem. C* **125**, 1282–1291 (2021).
14. Söngen, H. *et al.* Resolving Point Defects in the Hydration Structure of Calcite (10.4) with Three-Dimensional Atomic Force Microscopy. *Phys. Rev. Lett.* **120**, 116101 (2018).
15. Asakawa, H., Yoshioka, S., Nishimura, K. & Fukuma, T. Spatial Distribution of Lipid Headgroups and Water Molecules at Membrane/Water Interfaces Visualized by Three-Dimensional Scanning Force Microscopy. *ACS Nano* **6**, 9013–9020 (2012).
16. Kim, J., Zhao, F., Bonagiri, L. K. S., Ai, Q. & Zhang, Y. Electrical Double Layers Modulate the Growth of Solid–Electrolyte Interphases. *Chem. Mater.* **36**, 9156–9166 (2024).
17. Tian, C. S. & Shen, Y. R. Structure and charging of hydrophobic material/water interfaces studied by phase-sensitive sum-frequency vibrational spectroscopy. *Proc. Natl. Acad. Sci.* **106**, 15148–15153 (2009).
18. Velasco-Velez, J.-J. *et al.* The structure of interfacial water on gold electrodes studied by x-ray absorption spectroscopy. *Science* **346**, 831–834 (2014).
19. Li, C.-Y. *et al.* In situ probing electrified interfacial water structures at atomically flat surfaces. *Nat. Mater.* **18**, 697–701 (2019).
20. Toney, M. F. *et al.* Voltage-dependent ordering of water molecules at an electrode–electrolyte interface. *Nature* **368**, 444–446 (1994).

21. Poynor, A. *et al.* How Water Meets a Hydrophobic Surface. *Phys. Rev. Lett.* **97**, 266101 (2006).
22. Schwendel, D. *et al.* Interaction of Water with Self-Assembled Monolayers: Neutron Reflectivity Measurements of the Water Density in the Interface Region. *Langmuir* **19**, 2284–2293 (2003).
23. Li, C.-Y. *et al.* Unconventional interfacial water structure of highly concentrated aqueous electrolytes at negative electrode polarizations. *Nat. Commun.* **13**, 5330 (2022).
24. Montenegro, A. *et al.* Asymmetric response of interfacial water to applied electric fields. *Nature* **594**, 62–65 (2021).
25. Garcia, R. Interfacial Liquid Water on Graphite, Graphene, and 2D Materials. *ACS Nano* **17**, 51–69 (2023).
26. Yang, S. *et al.* Nature of the Electrical Double Layer on Suspended Graphene Electrodes. *J. Am. Chem. Soc.* **144**, 13327–13333 (2022).
27. Maccarini, M. *et al.* Density Depletion at Solid–Liquid Interfaces: a Neutron Reflectivity Study. *Langmuir* **23**, 598–608 (2007).
28. Utsunomiya, T., Yokota, Y., Enoki, T. & Fukui, K. Potential-dependent hydration structures at aqueous solution/graphite interfaces by electrochemical frequency modulation atomic force microscopy. *Chem. Commun.* **50**, 15537–15540 (2014).
29. Li, J. F. *et al.* Shell-isolated nanoparticle-enhanced Raman spectroscopy. *Nature* **464**, 392–395 (2010).
30. Ai, Q., Bonagiri, L. K. S., Farokh Payam, A., Aluru, N. R. & Zhang, Y. Toward Quantitative Interpretation of 3D Atomic Force Microscopy at Solid–Liquid Interfaces. *J. Phys. Chem. C* **129**, 5273–5286 (2025).
31. Dong, J.-C. *et al.* In situ Raman spectroscopic evidence for oxygen reduction reaction intermediates at platinum single-crystal surfaces. *Nat. Energy* **4**, 60–67 (2019).
32. Li, J. F. *et al.* Extraordinary enhancement of raman scattering from pyridine on single crystal Au and Pt electrodes by shell-isolated Au nanoparticles. *J. Am. Chem. Soc.* **133**, 15922–15925 (2011).
33. Zou, L., Li, L., Song, H. & Morris, G. Using mesoporous carbon electrodes for brackish water desalination. *Water Res.* **42**, 2340–2348 (2008).
34. Chakrabarti, M. H. *et al.* Application of carbon materials in redox flow batteries. *J. Power Sources* **253**, 150–166 (2014).
35. Gong, K., Du, F., Xia, Z., Durstock, M. & Dai, L. Nitrogen-Doped Carbon Nanotube Arrays with High Electrocatalytic Activity for Oxygen Reduction. *Science* **323**, 760–764 (2009).
36. Zhang, W. *et al.* Recent development of carbon electrode materials and their bioanalytical and environmental applications. *Chem. Soc. Rev.* **45**, 715–752 (2016).
37. M. Arvelo, D., R. Uhlig, M., Comer, J. & García, R. Interfacial layering of hydrocarbons on pristine graphite surfaces immersed in water. *Nanoscale* **14**, 14178–14184 (2022).
38. Benaglia, S. *et al.* Tip Charge Dependence of Three-Dimensional AFM Mapping of Concentrated Ionic Solutions. *Phys. Rev. Lett.* **127**, 196101 (2021).
39. Kilpatrick, J. I., Loh, S.-H. & Jarvis, S. P. Directly Probing the Effects of Ions on Hydration Forces at Interfaces. *J. Am. Chem. Soc.* **135**, 2628–2634 (2013).
40. Uhlig, M. R. & Garcia, R. In Situ Atomic-Scale Imaging of Interfacial Water under 3D Nanoscale Confinement. *Nano Lett.* **21**, 5593–5598 (2021).

41. Fukuma, T. & Garcia, R. Atomic- and Molecular-Resolution Mapping of Solid–Liquid Interfaces by 3D Atomic Force Microscopy. *ACS Nano* **12**, 11785–11797 (2018).
42. Kim, J., Zhao, F., Zhou, S., Panse, K. S. & Zhang, Y. Spectroscopic investigation of the structure of a pyrrolidinium-based ionic liquid at electrified interfaces. *J. Chem. Phys.* **156**, 114701 (2022).
43. Vidano, R. P., Fischbach, D. B., Willis, L. J. & Loehr, T. M. Observation of Raman band shifting with excitation wavelength for carbons and graphites. *Solid State Commun.* **39**, 341–344 (1981).
44. Kakihana, M. & Osada, M. Chapter 18 - Raman Spectroscopy as a Characterization Tool for Carbon Materials. in *Carbon Alloys* (eds. Yasuda, E. et al.) 285–298 (Elsevier Science, Oxford, 2003). doi:10.1016/B978-008044163-4/50018-8.
45. Kuhar, N., Sil, S., Verma, T. & Umapathy, S. Challenges in application of Raman spectroscopy to biology and materials. *RSC Adv.* **8**, 25888–25908 (2018).
46. Yu, Y. *et al.* New C–H Stretching Vibrational Spectral Features in the Raman Spectra of Gaseous and Liquid Ethanol. *J. Phys. Chem. C* **111**, 8971–8978 (2007).
47. Hurst, J. M., Li, L. & Liu, H. Adventitious hydrocarbons and the graphite-water interface. *Carbon* **134**, 464–469 (2018).
48. Larkin, P. J. Chapter 6 - IR and Raman Spectra–Structure Correlations: Characteristic Group Frequencies. in *Infrared and Raman Spectroscopy (Second Edition)* (ed. Larkin, P. J.) 85–134 (Elsevier, 2018). doi:10.1016/B978-0-12-804162-8.00006-9.
49. Tolman, N. L., Li, S., Zlotnikov, S. B., McQuain, A. D. & Liu, H. Characterization of environmental airborne hydrocarbon contaminants by surface-enhanced Raman scattering. *J. Chem. Phys.* **160**, 154708 (2024).
50. Larkin, P. J. Chapter 7 - General Outline for IR and Raman Spectral Interpretation. in *Infrared and Raman Spectroscopy (Second Edition)* (ed. Larkin, P. J.) 135–151 (Elsevier, 2018). doi:10.1016/B978-0-12-804162-8.00007-0.
51. Tainter, C. J., Ni, Y., Shi, L. & Skinner, J. L. Hydrogen Bonding and OH-Stretch Spectroscopy in Water: Hexamer (Cage), Liquid Surface, Liquid, and Ice. *J. Phys. Chem. Lett.* **4**, 12–17 (2013).
52. Medders, G. R. & Paesani, F. Infrared and Raman Spectroscopy of Liquid Water through “First-Principles” Many-Body Molecular Dynamics. *J. Chem. Theory Comput.* **11**, 1145–1154 (2015).
53. Kananenka, A. A. & Skinner, J. L. Fermi resonance in OH-stretch vibrational spectroscopy of liquid water and the water hexamer. *J. Chem. Phys.* **148**, 244107 (2018).
54. Shen, L. *et al.* Interfacial Structure of Water as a New Descriptor of the Hydrogen Evolution Reaction. *Angew. Chem. Int. Ed.* **59**, 22397–22402 (2020).
55. Scatena, L. F., Brown, M. G. & Richmond, G. L. Water at Hydrophobic Surfaces: Weak Hydrogen Bonding and Strong Orientation Effects. *Science* **292**, 908–912 (2001).
56. Ji, N., Ostroverkhov, V., Tian, C. S. & Shen, Y. R. Characterization of Vibrational Resonances of Water-Vapor Interfaces by Phase-Sensitive Sum-Frequency Spectroscopy. *Phys. Rev. Lett.* **100**, 096102 (2008).
57. Murphy, W. F. & Bernstein, H. J. Raman spectra and an assignment of the vibrational stretching region of water. *J. Phys. Chem.* **76**, 1147–1152 (1972).
58. Paolantoni, M., Lago, N. F., Albertí, M. & Laganà, A. Tetrahedral Ordering in Water: Raman Profiles and Their Temperature Dependence. *J. Phys. Chem. A* **113**, 15100–15105 (2009).

59. Qiao, M.-X., Zhang, Y., Zhai, L.-F. & Sun, M. Corrosion of graphite electrode in electrochemical advanced oxidation processes: Degradation protocol and environmental implication. *Chem. Eng. J.* **344**, 410–418 (2018).
60. Kumeda, T. *et al.* Surface Extraction Process During Initial Oxidation of Pt(111): Effect of Hydrophilic/Hydrophobic Cations in Alkaline Media. *J. Am. Chem. Soc.* **146**, 10312–10320 (2024).
61. Ataka, K., Yotsuyanagi, T. & Osawa, M. Potential-Dependent Reorientation of Water Molecules at an Electrode/Electrolyte Interface Studied by Surface-Enhanced Infrared Absorption Spectroscopy. *J. Phys. Chem.* **100**, 10664–10672 (1996).
62. Chattopadhyay, A. & Boxer, S. G. Vibrational Stark Effect Spectroscopy. *J. Am. Chem. Soc.* **117**, 1449–1450 (1995).
63. Andrews, S. S. & Boxer, S. G. Vibrational Stark Effects of Nitriles I. Methods and Experimental Results. *J. Phys. Chem. A* **104**, 11853–11863 (2000).
64. Villo, P., Shatskiy, A., Kärkäs, M. D. & Lundberg, H. Electrosynthetic C–O Bond Activation in Alcohols and Alcohol Derivatives. *Angew. Chem. Int. Ed.* **62**, e202211952 (2023).
65. Gagyí Palffy, E., Starzewski, P., Labani, A. & Fontana, A. Electrochemical reduction of polyaromatic compounds. *J. Appl. Electrochem.* **24**, 337–343 (1994).
66. King, J. F. & Mitch, W. A. Electrochemical reduction of halogenated organic contaminants using carbon-based cathodes: A review. *Crit. Rev. Environ. Sci. Technol.* **54**, 342–367 (2024).
67. Bewig, K. W. & Zisman, W. A. The Wetting of Gold and Platinum by Water. *J. Phys. Chem.* **69**, 4238–4242 (1965).
68. Park, J. Y. How titanium dioxide cleans itself. *Science* **361**, 753–753 (2018).
69. Grundner, M. & Jacob, H. Investigations on hydrophilic and hydrophobic silicon (100) wafer surfaces by X-ray photoelectron and high-resolution electron energy loss-spectroscopy. *Appl. Phys. A* **39**, 73–82 (1986).
70. Zhou, S., Panse, K. S., Motevaselian, M. H., Aluru, N. R. & Zhang, Y. Three-Dimensional Molecular Mapping of Ionic Liquids at Electrified Interfaces. *ACS Nano* **14**, 17515–17523 (2020).
71. Bonagiri, L. K. S. *et al.* Real-Space Charge Density Profiling of Electrode–Electrolyte Interfaces with Angstrom Depth Resolution. *ACS Nano* **16**, 19594–19604 (2022).
72. Panse, K. S. *et al.* Innermost Ion Association Configuration Is a Key Structural Descriptor of Ionic Liquids at Electrified Interfaces. *J. Phys. Chem. Lett.* **13**, 9464–9472 (2022).
73. Payam, A. F., Martin-Jimenez, D. & Garcia, R. Force reconstruction from tapping mode force microscopy experiments. *Nanotechnology* **26**, 185706 (2015).
74. Hölscher, H. Quantitative measurement of tip-sample interactions in amplitude modulation atomic force microscopy. *Appl. Phys. Lett.* **89**, 123109 (2006).